ACS NANO

www.acsnano.org

Colloidal 2D Layered SiC Quantum Dots from a Liquid Precursor: Surface Passivation, Bright Photoluminescence, and Planar Self-Assembly

Salim A. Thomas, Naif S. Alharthi, Reed J. Petersen, Ahmed Aldrees, Sakurako Tani, Kenneth J. Anderson, Joseph Granlie, Todd A. Pringle, Scott A. Payne, Yongki Choi, Dmitri S. Kilin, and Erik K. Hobbie*

Cite This: *ACS Nano* 2024, 18, 26848−26857

Read Online

ACCESS | Metrics & More | Article Recommendations | Supporting Information

ABSTRACT: **We report the bottom-up synthesis of colloidal two-dimensional (2D) layered silicon carbide (SiC) quantum dots with a cubic structure, lateral size of 5−10 nm, ⟨110⟩ exfoliation to few atomic layers, and surface passivation with 1-dodecene. Samples shielded from oxygen and plasma-annealed for purity exhibit narrow blue photoluminescence (PL) with quantum yields (QYs) over 60% in exceptional cases, while unshielded nanocrystals (NCs) exhibit broad blue/green/white PL with 10−15% QY. The latter scenario is attributed to excess surface carbon and oxygen accrued during synthesis and processing, with size separation through ultracentrifugation revealing size-dependent impurity emission. In contrast, the shape of the bright narrow blue PL shows little variation with NC size, while in both scenarios, the maximum QY occurs near four atomic layers. When dried under heat, the disk-like NC suspensions are observed to aggregate into microscale domains, with further self-assembly into planar superlattice domains with common crystalline orientation. The results are compared with photophysical simulations and bring clarity to the broad emission commonly reported for top-down approaches, while inspiring bottom-up schemes directed at improved material quality.**

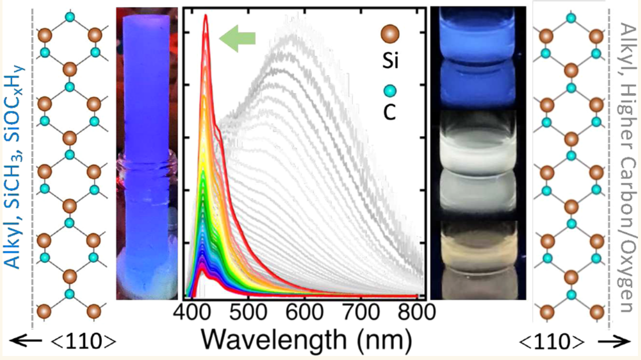

KEYWORDS: *silicon carbide, nanocrystals, layered materials, photoluminescence, self-assembly*

Two-dimensional (2D) layered materials and semiconductors, such as graphene, hexagonal-boron nitride, and the various transition metal dichalcogenides, are of current interest for a range of scientific questions related to a variety of potential electronic and optoelectronic applications.[1−4] As a wide-band gap semiconductor, silicon carbide (SiC) boasts many exemplary physical attributes of its own, with perhaps the most notable being physical hardness. Silicon carbide also exhibits a variety of crystalline polymorphs, and although 2D monolayer honeycomb SiC was theoretically predicted to be a stable phase nearly a decade ago,[5] it has only recently been realized, specifically by thermally annealing ultrathin (<3 nm) transition metal carbide films on the Si-terminated face of 4H SiC in an inert atmosphere.[6] In part, this longstanding challenge stems from the fact that unlike graphitic carbon, silicon carbide exhibits no known layered phase and does not naturally exfoliate using top-down approaches,[7−9] which by necessity are harsh, corrosive, and oxidizing.

Among the many emerging potential applications for nanostructured SiC, some of the most compelling ones relate to photonics and quantum technologies,[10] which is a direct consequence of the outstanding characteristics of the material. As is often the case, accessing these features in a colloidal "quantum dot" platform has the potential to enable fluid processing and the associated technologies. In contrast to the commonly employed top-down approaches—which produce a strongly oxidized material with a degree of intrinsic solubility in polar solvents—"bottom-up" synthetic schemes targeting nanocrystalline and microcrystalline SiC are much less

Received: June 17, 2024
Revised: August 29, 2024
Accepted: September 6, 2024
Published: September 17, 2024

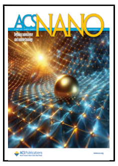

https://doi.org/10.1021/acsnano.4c08052
ACS Nano 2024, 18, 26848−26857

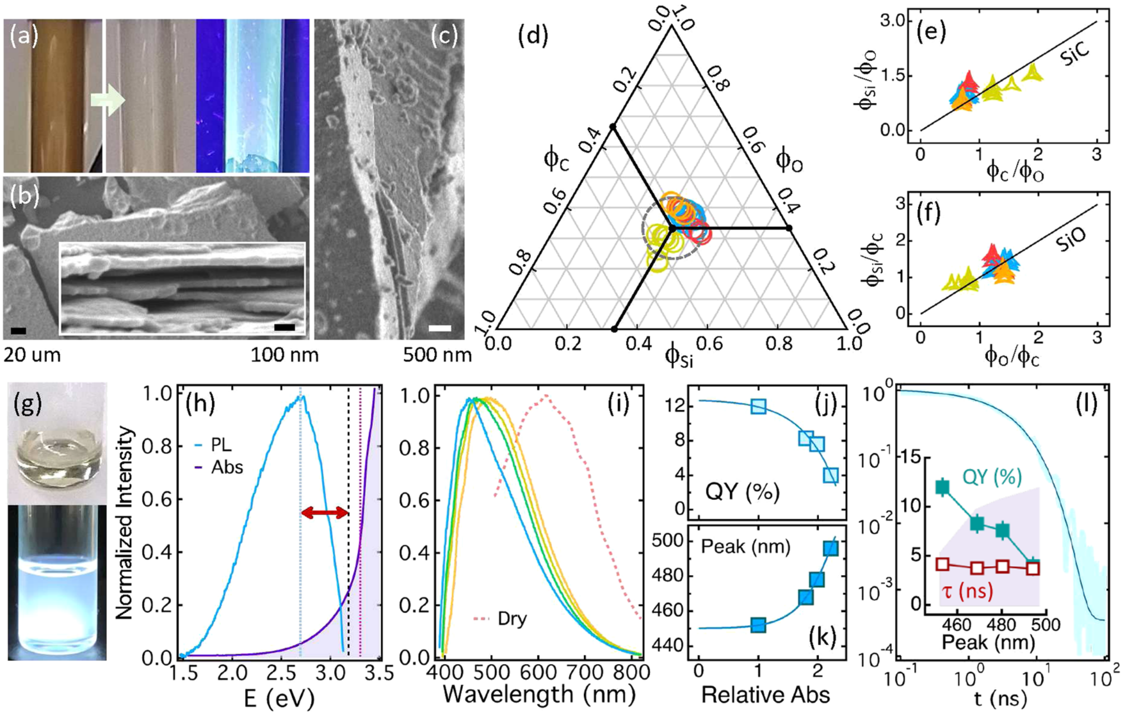

Figure 1. (a) Portion of a reactor immediately after synthesis (left) and after 24 h in air under ambient (middle) and UV (right) light. (b) SEM image of layered morphology (20 μm scale), where the inset shows the stratified deposit (100 nm scale). (c) SEM image of raw powder (500 nm scale) showing terraced layers. (d) Composition in the Si/C/O triangle for the exposed raw material from across the reactor with (e) Si vs C content (normalized by O) and (f) Si vs O content was 0 equiv. (normalized by C). (g) Ligand-passivated colloid under ambient (top) and UV (bottom) light. (h) PL spectrum (12% QY) vs photon energy, where the filled purple curve is absorption, the purple line is excitation, and the black dashed line is the Tauc gap (red arrow indicates effective Stokes shift). (i) Colloid PL spectra with increasing concentration from dilute colloid (blue) to dried film (red). (j) QY and (k) PL peaks as a function of increasing concentration (relative absorption). (l) Typical PL decay curve with a stretched-exponential fit, where the inset shows QY and lifetime vs PL peak as a function of increasing concentration (purple).

common and more recent.[11−17] The resulting SiC nanocrystals (NCs) can exhibit broad visible photoluminescence (PL), but this feature is not universally observed and its precise nature remains poorly understood. When present, it resembles the broad blue/green/white emission commonly reported for top-down approaches, with reported quantum yields (QYs) of ≤ 17%.[10,18−27] Although some of these studies suggest quantum confinement, multiple types of surface impurities have also been implicated as the probable source of the PL.[22] Indeed, impurity and/or defect emission in general is what currently defines the photophysical landscape of all forms of crystalline SiC, across the visible to the NIR region.[10,18−32] The commercial potential of these materials is thus highly dependent on our ability to control and engineer such features.

Here, we report the bottom-up synthesis of 2D layered SiC quantum dots from the liquid precursor tetramethylsilane (TMS). The plate-like NCs have a cubic (β) SiC structure, lateral size of around 10 nm, and ⟨110⟩ exfoliation to 1−6 atomic layers. Notably, the NCs are surface-passivated with 1-dodecene for colloidal stability in organic solvents, which allows us to use size separation through density-gradient ultracentrifugation (DGU) as a characterization tool. Samples shielded from oxygen and plasma-annealed prior to passivation show narrow blue PL with QYs near 60% in exceptional cases, while unshielded NCs universally exhibit broad blue/green/white PL with 10−15% QY. In the second scenario, the PL resembles the broad fluorescence commonly reported for nanoscale SiC, with DGU revealing size-dependent impurity emission associated with excess surface carbon and oxygen accrued during synthesis and processing. In contrast, the bright narrow blue PL has not been previously reported and is linked to a much cleaner SiC surface. Surprisingly, the bright emission exhibits little variation with NC size, implicating a highly optimized impurity/defect PL mechanism, which we suggest includes intrinsic surface effects in "clean" but overconfined SiC. For both scenarios, the maximum QY occurs near four atomic layers, which we suggest represents the optimal combination of two absorbing base layers and two emitting surface layers. The NCs are also observed to phase-separate under modest heat, with self-assembly into square "discotic superlattice" domains with common underlying NC orientation. Our results are compared with simulations of the PL from disk-shaped SiC NCs and bring much needed clarity to the nature of the blue/green/white emission commonly reported for top-down approaches. At the same time, the findings illuminate potential pathways to "bottom-up" materials with exceptional properties.

An important aspect of this work is the surface passivation of SiC NCs through simple thermal hydrosilylation with 1-dodecene, which renders the quantum dots soluble in organic solvents and enables polymer blending and liquid-phase processing. To the best of our knowledge, the chemical grafting of SiC nanostructures with short organic chains has only been performed on acid-processed SiC materials,[33,34] which invariably will have highly oxidized surfaces.[35] In contrast, simulations suggest that pure H-termination leads to more desirable photophysical attributes,[36] and ligand passivation likely plays a critical role in both the quality of

https://doi.org/10.1021/acsnano.4c08052

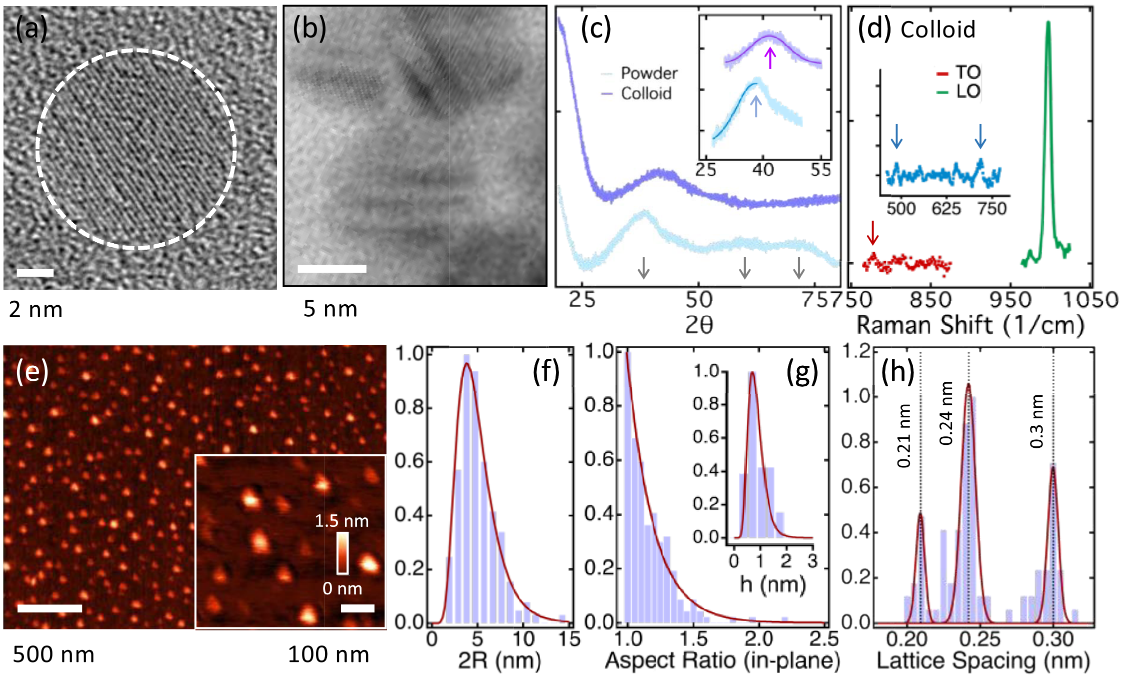

Figure 2. (a) TEM image of an individual NC (2 nm scale). (b) TEM image of colloidal NCs showing Moiré fringes from superposed plates (5 nm scale). (c) XRD profiles of raw powder and the resulting colloid, where the peaks indicated by arrows correspond to the $\langle 111\rangle$, $\langle 220\rangle$, and $\langle 311\rangle$ directions of nanocrystalline β-SiC (from left to right). The inset shows the Scherrer fits used to deduce plate thickness h (0.82 nm for raw flakes, 0.83 nm for colloid), with the indicated peaks corresponding to lattice spacings of 0.23 nm (powder) and 0.22 nm (colloid). (d) Raman spectrum of colloidal NCs showing only the LO peak (green), where the red arrow is the anticipated location of the TO peak, and the arrows at 480 and 720 cm^{-1} (inset) indicate the anticipated positions of a-Si and ligand peaks, respectively. (e) AFM image of size-purified colloidal NCs spin-coated on a c-Si wafer (500 nm scale), where the inset shows a higher magnification image with height scale. (f) Lateral size histogram from TEM with log-normal fit. (g) Histogram of the aspect ratio with an exponential fit, where the inset shows total AFM height (thickness) distribution of a parent compiled from several of its DGU fractions. (h) Lattice spacing histogram from TEM ($\langle 1\bar{1}0\rangle$, $\langle 1\bar{1}1\rangle$, $\langle 001\rangle$ planes, from left to right).

the PL we are able to achieve and the unusual self-assembly that these nanomaterials exhibit. In some ways, the NCs are SiC analogs of the popular carbon dots,[37−44] particularly those built on layered graphene platforms. However, the use of SiC as the "core" material in a bottom-up synthetic methodology demands a different environment and hence a very different approach.

RESULTS AND DISCUSSION

We synthesize the SiC NCs using a nonthermal plasma reactor and the liquid precursor tetramethylsilane (TMS) in a manner that resembles our process for making ligand-passivated 3D Si NCs from cyclohexasilane[45,46] but with important differences. Most notably, the SiC dots form on the wall of the reactor in a layered bulk form, requiring collection and sonication-assisted exfoliation of the flake-like material prior to surface passivation. As we demonstrate here, TMS is in some ways an nonideal precursor for luminescent SiC NCs due to its intrinsic stoichiometric imbalance (4:1 C:Si), but it has been used recently for bottom-up nanoscale SiC syntheses and thus represents a valuable point of reference.[12,13,16] In contrast to our previously synthesized 3D SiC NCs, which were unpassivated and nonluminescent,[16] the dots made here are surface-passivated through hydrosilylation with 1-dodecene, which enables nanoscale colloidal dispersion and permits DGU as a characterization tool.[47−49] This purification step is critical to revealing not just the shape and size of the NCs but the nature of the PL as well. Details related to synthesis and processing can be found in the Materials and Methods. Briefly, we employ flow rates marginally greater than those previously used to make small (2−3 nm diameter) SiC NCs[16] but in much narrower reactors. Under these conditions, there is no filter deposition of nanoscale particulates but only wall deposition, which is critical to the layered structure of the raw SiC material.

Figure 1a shows a portion of a reactor immediately after synthesis (left) and again after 24 h in air (right) under both ambient and UV (365 nm LED) light. The deposit lightens in appearance and acquires white PL with a blue/green tint upon exposure to air, which we attribute to the oxidation of H-terminated surface Si in wide-band gap SiC. After removing the bulk material from the reactor walls with heat, scanning electron microscopy (SEM) reveals a layered sheet-like morphology (Figure 1b,c), where additional images can be found in Figure S1. The layered structure of the raw SiC flakes of interest is evident as stepped terraces in Figure 1c. Energy dispersive X-ray spectroscopy (EDS) on such a raw exposed material (Figure 1d) reveals equal fractions of Si, C, and O, where the tie lines in Figure 1d indicate 1:1:1 composition. Figure 1e shows Si content vs C content (normalized by O) and Figure 1f shows Si content vs O content (normalized by C), where both lines have slope 1. The EDS data indicate SiOC for exposed flakes, with Raman spectroscopy identifying the spherical inclusions (Figure 1b) to be amorphous silicon (a-Si), as discussed further below.

After tip sonication in mesitylene to exfoliate the bulk layered material, the resulting nanoflakes readily undergo thermal hydrosilylation with 1-dodecene to form a stable

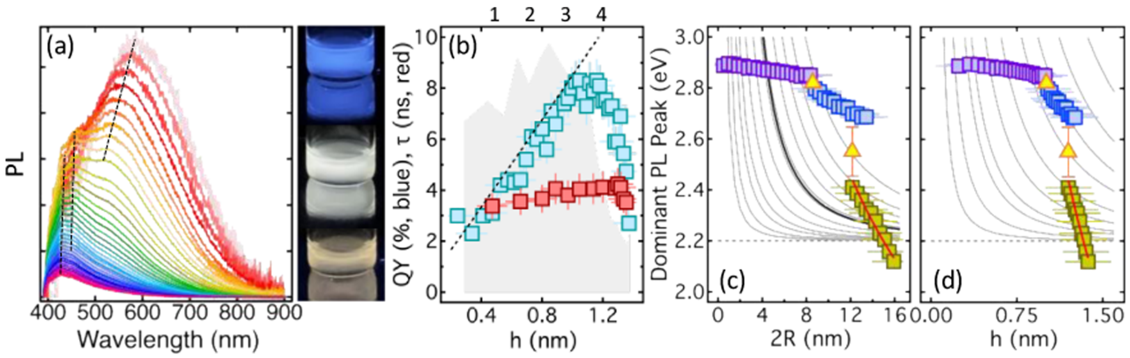

Figure 3. (a) DGU fractions from a 10% QY parent showing three distinct emission channels as a function of size (dashed black lines), with fractions exhibiting blue, green, and orange PL ($f2$, $f28$, $f36$, right panel). (b) QY and lifetime vs NC thickness, with optical absorption shown in light gray (the dashed line is the NC aspect ratio, $2R/h$) and where the upper axis is the approximate layer number. (c) Dominant PL peak as a function of $2R$ where gray curves are typical confinement profiles and yellow triangles denote the mean value of the corresponding jump. The heavy black curve is from ref16. (d) Dominant PL peak as a function of h. The red curves in the last two panels are the heuristic power-law fits detailed in the text.

colloid that retains the broad emission (Figure 1g). Typical PL/absorption spectra are shown in Figure 1h and indicate a large Stokes shift. Interestingly, the PL red-shifts with increasing concentration such that the emission from a dried film is red. We note that samples shielded from air throughout synthesis and processing did not show this trend, which we attribute to concentration effects (e.g., broad PL and self-absorption) and the interaction of the red-emitting oxygen-containing surface groups detailed below. As is often observed for quantum dots, the PL QY drops as the concentration increases (Figure 1j,k), with dilute suspensions from exposed flakes typically having QYs near 10−15%. In response to pulsed UV excitation, the time-dependent PL intensity, $I(t)$, exhibits a stretched exponential decay, $I(t) = I_0 \exp[-(t/\tau)^{\alpha}]$ (Figure 1l), with typical stretching exponents (α) of 0.6 to 0.7, indicating a broad distribution of emitting states. Although the QY drops with increasing concentration, the PL lifetime (τ) is constant at near 4−5 ns. Additional information related to processing, exposure, and QY for these unshielded materials can be found in Figure S2.

The shape and crystallinity of the colloidal NCs were evaluated with transmission electron microscopy (TEM), X-ray diffraction (XRD), and atomic force microscopy (AFM), as detailed in Figure 2, the Materials and Methods, and the Supporting Information. Individual dots and their stacked layers can be resolved with TEM (Figure 2a,b), where some stacking occurs because of self-assembly when the grids are dried (Figure S3), as detailed further below. The XRD spectra are smeared due to the thin nature of the NCs (Figure 2c), but the lattice spacing of the colloid (0.22 nm) is slightly smaller than that of the powder (0.23 nm), and Scherrer fits of the ⟨111⟩ peak give a NC thickness (h) near 0.8 nm for both powder and colloid (inset, Figure 2c). To directly assess NC thickness, parent suspensions were size-purified with DGU, and dilute fractions were spin-coated from toluene/hexane onto polished wafer silicon, dried under vacuum at 200 °C, and evaluated with AFM. A typical AFM image is shown in Figure 2e and demonstrates the 2D disk-like shape of the NCs. Representative lateral size/shape (TEM) and thickness (AFM) distributions for a parent suspension are shown in Figure 2f−g, where the latter is obtained as a sum over thickness distributions for the fractions. Lattice spacings based on TEM (Figure 2h) agree with XRD and are consistent with the ⟨110⟩ exfoliation of cubic (β) SiC, which exposes the stoichiometrically mixed face as the dominant surface. The structural picture is thus alkyl-functionalized few layer-thick crystalline SiC disks of 5−10 nm lateral size with a roughly circular shape (in-plane aspect ratio: ∼1) and 5:15 out-of-plane aspect ratio (defined as $2R/h$).

Raman spectra of the ligand-passivated SiC NC flakes show a strong longitudinal optical (LO) mode (Figure 2d), where the peak (∼990 cm^{-1}) is blue-shifted 20 cm^{-1} from values reported for bulk and 3D nanoscale SiC (typically, ∼ 970 cm^{-1}). Optical phonon splitting is suppressed in quasi-2D zinc-blende systems,[50,51] with the LO collapsing onto the TO due to Coulomb screening effects in 2D. However, several factors could influence the relative intensity here, and this question will be explored in detail elsewhere. For the present purposes, Raman spectroscopy provides an added confirmation of crystallinity, where additional spectra can be found in Figure S4. For the high-QY suspensions detailed further below, Raman spectra of the raw flakes prior to passivation show a weak but discernible TO mode at 780 cm^{-1}, along with longitudinal acoustic (LA) features associated with disordered SiC and other crystalline SiC polytypes. However, such features do not appear in the colloid, suggesting that they do not survive passivation and processing. For low-QY colloids, the disordered SiC LA peak at 680 cm^{-1} dominates the raw-flake Raman spectrum.

The reduced dimensionality of the NCs becomes immediately evident in DGU. Sedimentation velocity scales as R^2 for a sphere but as Rh for a disk, and $h < 1$ nm implies spinning at least twice as long (over 40 h, in this case) compared to what we typically do for 3D Si NCs to get desirable size separation (see the Materials and Methods for details). Sizing data for DGU fractions based on TEM (lateral size $2R$) and AFM (thickness h) can be found in Figure S5. Figure 3a describes the PL characteristics of the fractions, which show three broad but distinct emission channels with increasing size (fraction number f or sedimentation depth), with the longest wavelength channel showing a red shift suggestive of confinement and where the origin of each of these is detailed below. The QY, lifetime (Figure S6), and optical absorption of the fractions are plotted as a function of effective h in Figure 3b. Note that the QY of the parent in mesitylene was around 10%, but there is a slight drop when switching to toluene/hexane. Maximum QY occurs near $h \approx 1.1$ nm, which corresponds to four atomic layers accounting for the ligand (Materials and Methods), and

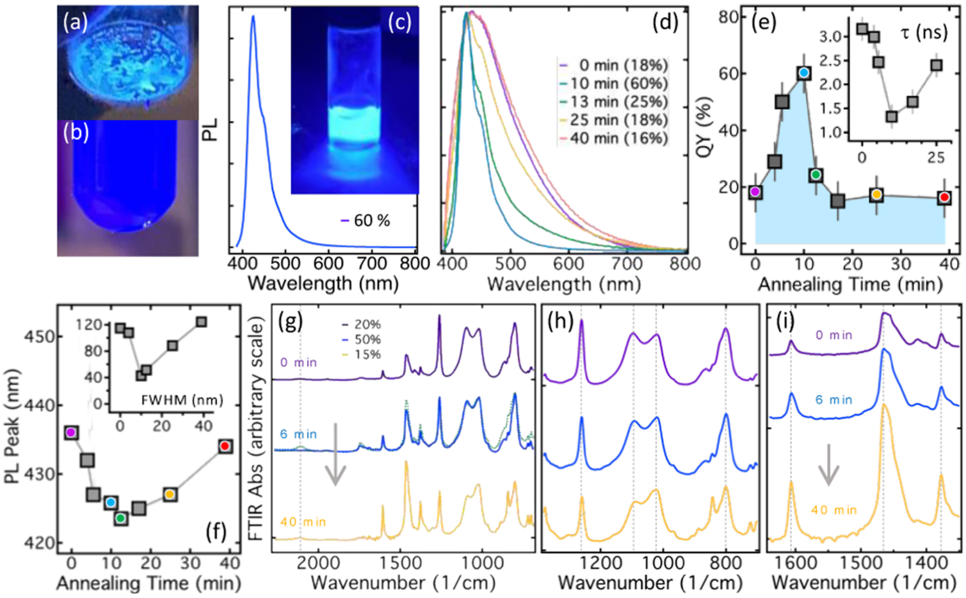

Figure 4. (a) Optimally luminescent raw flakes, (b) PL from the NC suspension after sonication, and (c) final passivated colloid, with 60% QY and relatively narrow line width. The PL from the vial is saturating the digital camera. (d) PL spectra of the best samples obtained at each annealing time. (e) Highest QY vs annealing time, where the inset shows lifetime vs annealing time. (f) PL peak wavelength and (inset) fwhm vs annealing time. (g) Expanded view of FTIR spectra as a function of annealing time (arrow indicates longer annealing), where the vertical dashed line indicates the SiH peak (2116 cm^{-1}). (h) SiC and SiO FTIR bands at varied annealing times, where the vertical dashed lines (left to right) are SiCH$_3$ (1256 cm^{-1}), SiOC$_x$H$_y$ (1090, 1020 cm^{-1}), and SiC (800 cm^{-1}). (i) FTIR peaks associated with surface passivation, where the vertical dashed lines (left to right) are SiC$_x$H$_y$ (1607 cm^{-1}), bound ligand (1460 cm^{-1}), and SiOC$_x$H$_y$ (1375 cm^{-1}). All spectra are normalized to the SiC peak at 800 cm^{-1}.

$2R \approx 10$ nm (which corresponds to the NC aspect ratio of 10, where the dashed line in Figure 3b shows the out-of-plane aspect ratio vs h). Over the same range of thicknesses, the lifetime is relatively constant at 4–5 ns. These low-QY parents have a visible tint, with optical absorption providing a measure of mass distribution across the gradient (light-gray profile, Figure 3b), although the unbound ligand from the parent likely contributes to absorption for $f \leq 10$, where the QY is thus likely understated.

Figures 3c,d compares the dominant PL peak with quantum confinement trends. Data in Figure 3c are plotted with the expression $E = E_0 + A/(2R)^2$ for $0.5 \leq A \leq 50$, with $E_0 = 2.2$ eV for β-SiC. The heavy black curve is $A = 14.5$ as suggested by recent size-dependent absorption trends for nonluminescent SiC NCs.[16] For comparison, typical values from Si NCs are $A \approx 3$–4.[45] None of the trends in Figure 3c are consistent with confinement, although the jumps between dominant peaks (yellow markers) appear to be consistent with $A = 50$. The data in Figure 3d are compared with the expression $E = E_0 + A/h^2$ for $0.01 \leq A \leq 1.5$, and although both the middle dataset and the jumps between dominant peaks fall on the trend for $A \approx 0.6$, the overall size dependence is not consistent with accepted confinement trends. The Bohr radius of β-SiC is 2 nm, which is well below the typical $2R$ values here, implying that R is not a dimension of confinement. In contrast, $h \leq 1$ nm is well below the Bohr radius, and lateral confinement is therefore quite strong. The correct physical picture is thus size-dependent impurity/surface emission in the limit of strong confinement (Figure S7). Phenomenologically, the red-shifting data scale as surface area per unit volume, h^{-1} or $R^{-1/2}$ (red curves, Figure 3c,d) using $R/h \sim h$ (dashed line, Figure 3b).

A richer picture of the nature of the PL emerges when the dots are shielded from oxygen throughout synthesis, processing, and passivation with brief annealing in the plasma prior to processing/passivation. In the reactor, TMS decomposes to form SiC clusters that deposit on the walls along with excess carbon. In the plasma, hydrogen, sourced from both the carrier gas and TMS, removes this excess carbon and adjusts the composition profile, allowing the material to "anneal" as it grows to a final thickness of several tens of microns. A strong flow at the reactor surface causes the deposit to become stratified (Figure 1b,c), with hydrogen passivating dangling Si and C bonds, enabling exfoliation and hydrosilylation. Growth is facilitated by deposition/sublimation under shear without the presence of a liquid SiC phase. The inherent 4:1 imbalance of TMS makes annealing a crucial step. Plasma annealing fine-tunes the stoichiometry of the outer surfaces: if it is too brief, excess carbon remains; if it is too prolonged, excess silicon becomes predominant. The presence of amorphous silicon (a-Si) spherical inclusions in the raw flakes (Figure S4) indicates regions of intense annealing, where such large features do not survive processing and passivation. Figure 4a–d displays the resulting photoluminescence (PL) for various annealing durations, defined as the total time in the plasma with only the carrier gas and no precursor. The data in Figure 4d correspond to the highest quantum yields (QYs) of the passivated colloid for a given annealing time and suggest that an optimal annealing time is around 5–10 min for a 2 h run.

Figure 4e,f further details the PL as a function of annealing. The highest QY, shortest lifetime (Figure S8), bluest PL, and narrowest line width all coincide with the optimal time of 5–10 min, where TEM images of the high-QY colloid can be found in Figure S9. These high-QY suspensions are optically transparent (no visual tint), consistent with high-purity SiC (Figure S10). The lifetime trend for these parent suspensions

https://doi.org/10.1021/acsnano.4c08052
ACS Nano 2024, 18, 26848−26857

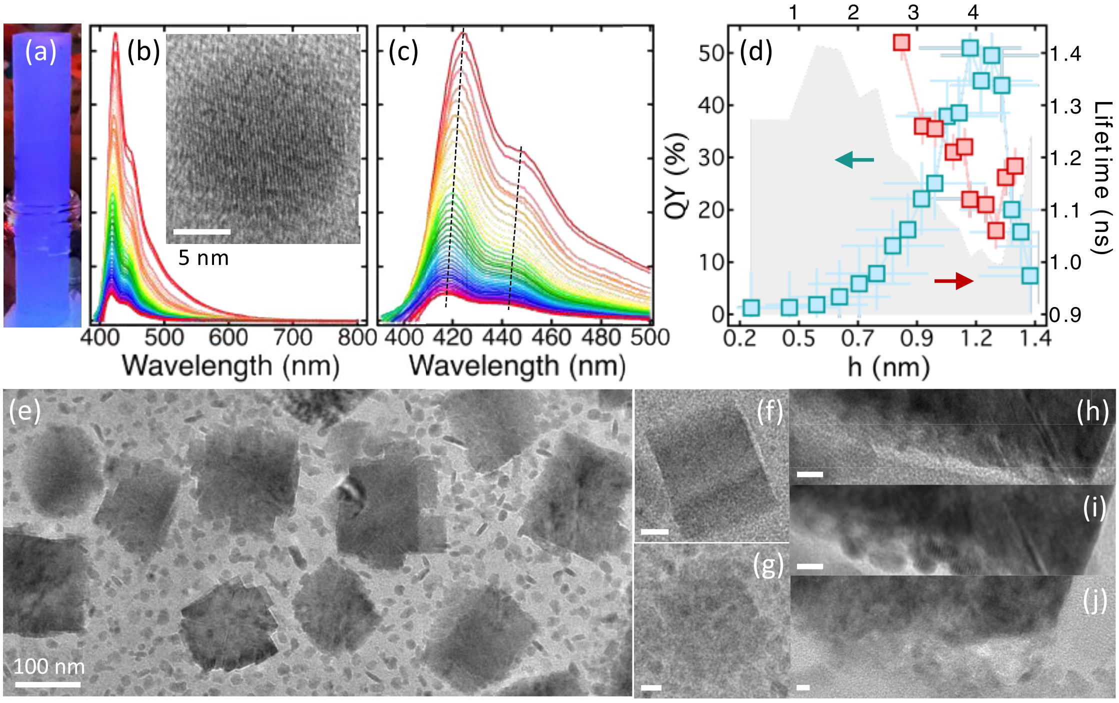

Figure 5. (a) PL from a postspin gradient of a high-QY parent. (b) Emission spectra from across the gradient, with NC thickness increasing with depth. The inset shows a TEM image of an individual disk-like NC from a high QY fraction (*f*26, *h* = 1.11 nm, 5 nm scale). (c) Expanded view of the size-resolved spectra in (b), with the two dominant emission channels showing little dependence on NC size/thickness. (d) QY (blue, left scale) and lifetime (red, right scale) vs NC thickness, where the light-gray profile is the optical absorption. The upper horizontal scale is the approximate layer number. (e) TEM image of the self-assembled planar "superlattice" coexisting with isolated individual disk NCs and small aggregates (100 nm scale). (f, g) NC domain "melting" in the TEM beam (10 nm scale) and (h−j) similar sequence for a NC domain edge (10 nm scale).

is revealing because it fully implicates defect/impurity emission. For core PL like the red/NIR emission observed from Si NCs,[45] long lifetime correlates with high QY. The opposite trend here reflects energy transfer to the surface emitter, with QY being the highest when the transfer rate (τ^{-1}) is maximum. The data in Figure 4d−f are summarized in Table S1.

Figure 4g−i shows colloid FTIR for varied annealing times and QYs, where spectra are normalized to the SiC peak at 800 cm^{-1}. Spectra for shorter annealing show strong narrow SiC, strong narrow $SiCH_3$, and strong symmetric SiOC, which diminish at longer annealing times (Figure 4g,h). For samples with the optimal annealing but lower QY (green dashed curve, Figure 4i, QY = 17%), FTIR implicates SiH in the colloid, consistent with incomplete exfoliation/passivation. The FTIR peak associated with the bound ligand (1460 cm^{-1}, the pure-ligand FTIR feature that is enhanced by hydrosilylation) increases with annealing time (Figure 4i), which is consistent with an increase in the number of available Si−H sites with the removal of carbon. Normalizing to the bound ligand peak instead, the overall carbon content decreases with annealing (Figure S13), and we suggest that high QY corresponds to the removal of C to the point of optimally balanced Si:C stoichiometry in the flakes—obviously a challenge with TMS—coupled with the highest possible degree of oxygen shielding. The outer surface of the material contacting the reactor is shielded from the plasma during deposition and will have a residual stoichiometric imbalance that requires annealing. The shoulder peak on SiC (~845 cm^{-1}) at 40 min annealing indicates $SiCH_3$ associated with surface "copolymers" of siloxane, consistent with the cumulative effects of trace oxygen in the plasma after extended annealing time.

A notable feature of the high-QY colloid is a lack of SiH, indicating near-complete hydrosilylation. This is different from Si NCs (Figure S12), which have roughly 50% ligand coverage,[45] but it can be rationalized by 50% carbon on the dominant equal-stoichiometric ⟨110⟩ face. X-ray photoelectron spectra (XPS) and additional FTIR spectra for the raw material, colloids, and pure ligand can be found in Figures S11 and S13, along with a table of FTIR peak assignments (Table S2). Based on FTIR, we link the primary PL peak (~420 nm) to $SiCH_3$ and $SiOCH_3$, where we suggest that the former will act as a surface recombination site in overconfined few-layer SiC and we attribute the secondary PL peak (~445 nm) to $SiOCH_2CH_3$ and $SiOCH_2CH_2CH_3$. The same two peaks that are apparent in the high-QY fractions are also present in the low-QY fractions (Figure 3), where they are just weaker and broader. A third red-shifting peak (~550 nm) emerges in the low-QY colloids that we assign to still higher order O and C. The results are in qualitative agreement with complementary simulations (Figure S14) that rely on density matrix dissipative dynamics, as described in detail elsewhere.[52] The simulation results suggest that pure hydrocarbon termination should give the highest QY (55%); however, the surface oxygen impurity $SiOCH_3$ is surprisingly bright (41.5% QY), which can be rationalized by a low degree of charge localization near the oxygen impurity, resulting in a minimal change in the nonradiative rate compared to intrinsic surface passivation.

Interestingly, the DGU assay looks quite different for the high-QY colloidal SiC NCs, where the PL color and spectral shape show little variation with size, instead resembling the parent (Figure 5a−c), but with a slightly smaller fwhm for the best fractions (∼35 nm). This is in marked contrast with the behavior presented in Figure 3. Nonetheless, the maximum QY again occurs near four atomic layers (Figure 5d) with a drop in QY on moving from mesitylene to the gradient solvents hexane/toluene. The low optical absorption of the highest-QY fractions reflects a high degree of SiC purity, with the mass in these fractions being significant as we demonstrate below with TEM. Note that while the QY generally increases as we progress from Figures 1 to 5, the lifetime gets progressively smaller, as might be expected for impurity/defect emission. Like the parent behavior depicted in Figure 4e, the lifetime measured for the high-QY fractions exhibits a minimum near the maximum QY (Figure 5d), where such effects are likely concealed by a broad distribution of impurities in Figure 3b.

Another striking feature of the suspensions is their self-assembly, as detailed in Figure 5e−k for a fraction near the maximum QY (Figure 5d, *f*26, $h = 1.15$ nm). Like other colloidal NC suspensions, the NCs form aggregates when dried at sufficient concentration. Although a detailed study will be presented elsewhere, here, the anisotropic clusters or planar domains coexist with individual dots (Figure 5e). Depositing an entire fraction onto a TEM grid and drying at ambient temperature under vacuum, for example, leads to an unimaginable hazy grid covered with the material, but simply heating the grid under a vacuum for 48 h transforms the material into coexisting structures like those shown here. The aggregates initially assemble as amorphous clusters that in some instances then further evolve into thin faceted planar domains, of which additional TEM images can be found in Figure S15. These structures "melt" back to the constituent NC disks under sufficient electron beam intensity, as shown in Figure 5f−h for a whole domain and Figure 5i,j for the edge of a larger domain.

Notably, some of the planar assemblies have common underlying NC crystalline orientation, as demonstrated in Figure S16, where this alignment occurs during assembly and is consistent with a short-range interparticle potential that mirrors the asymmetry of the underlying crystalline lattice.[53] Ligand passivation is obviously critical to the process. Although the exposed ⟨110⟩ faces have uniform ligand coverage, the edges will be heterogeneous. Pure-carbon edges will ideally have short hydrocarbon terminations, while those with pure silicon are presumably ligand-decorated. Similar edges will thus be attractive in the short range, which could help the anisotropic dots assemble into globally ordered domains. The residual solvent in the self-assembled sheets likely plays a role in NC mobility, as well. After 48 h at 100−200 °C, large planar aggregates show signs of solvent boiling in the focused electron beam, indicative of the intercalated solvent within the assemblies despite their thermal history. The results will be of general interest across the broader field of nanoparticle interactions and NC self-assembly.[54]

CONCLUSIONS

In conclusion, we report the bottom-up synthesis of colloidal SiC quantum dots with ⟨110⟩ exfoliation to few atomic layers and surface passivation with 1-dodecene. The purest materials exhibit narrow blue PL with QYs over 60% in exceptional samples, making these intrinsically nontoxic NCs of potential interest for biolabeling and display applications. This benchmark was accomplished through a combination of oxygen shielding and plasma processing targeting stoichiometric purity. Regardless of purity, our measurements suggest that the optimum QY occurs at around four atomic layers, which corresponds to the somewhat intuitive scenario of two emitting surface layers encapsulating two inner absorbing layers. Our results bring clarity to the long-standing question regarding the nature of blue/green/white PL from SiC NCs while empowering other SiC shapes and sizes with exemplary blue/green emission.

As we demonstrate here, surface chemistry is critical, and future approaches should target stoichiometrically balanced precursors with more reliably stringent oxygen shielding, which we are currently investigating. Although blue and green surface PL can be achieved in Si NCs through the appropriate choice of structured ligands,[55] the materials described here rely only on simple ligands and thermal passivation to achieve narrow blue PL from an anisotropic NC geometry. From the perspective of surface or near-surface Si, the results suggest that optimal processing corresponds to an equal balance of alkyl functionalization, $SiCH_3/SiOC_xH_y$ termination, and an absence of SiH reflecting a high degree of exfoliation. In contrast, a higher carbon content creates stronger absorption with weaker and broader emission, while a higher surface Si content reduces both the extent of the SiC "core" and the prevalence of the desirable emitting surface functionalities.

The thermally driven self-assembly of the disk-shaped NCs into planar superlattice structures with a common crystalline orientation is also striking. Mobility would seem to be key, with the ligand and residual solvent likely playing a critical role. Finding a common NC orientation for two facially stacked disks would seem to be as simple as a rotation, and correct edge-to-edge assembly for the irregularly shaped plates could conceivably follow from this. The fact that domains of the somewhat irregularly shaped NCs can assemble into planar shapes with sharp well-defined edges is intriguing, and we expect this work to motivate insights into NC self-assembly in general. Ligand passivation and associated ligand effects, such as the presence of the intercalated solvent and unbound ligand, are no doubt critical to this process, given that the NCs have a surface-to-volume ratio that scales as h^{-1} for small h.

MATERIALS AND METHODS

NC Synthesis and Processing. Borosilicate glass reactors (38 cm total length; 20 cm upper length with 0.94 cm OD, 0.56 cm ID; 17.8 cm bottom length with 2.54 cm ID, 2.06 cm OD, 2.54 cm widening interval) were placed in a base bath (250 g of KOH, 4 L of isopropyl alcohol, 1 L of DI water) for 16 h, rinsed in DI water for 5 min, and dried in an oven at 150 °C for 30 min. Treatment of the reactor in this manner is critical. For longer base bath immersion times, the flakes fall off during deposition, while for shorter times, they resist removal. After installation, the reactor tube was purged three times for 15 min using 95/5 Ar/H_2, which also serves as the carrier gas. The reactor was then left under vacuum for 5 h, and seals/pressures were tested/monitored to minimize leaks before initiating synthesis. The positive electrode was placed 14 cm from the upstream disconnect and 3.5 cm above where the reactor widens, with the ground electrode 1.3 cm below. In this configuration, the plasma arcs to the top disconnect rather than the ground electrode, which instead moderates the plasma shape.

The flakes were synthesized by flowing 3 sccm carrier gas through a bubbler of TMS with 40 sccm carrier gas added to the mixture before the plasma (40 W at 13.56 MHz). The pressure in the reactor was held constant at 5.8 Torr with a gate valve. Negligible aerosolized material forms under these conditions. Instead, layered material forms on the reactor walls in the upstream plasma, with a working sample collection length of around 5 cm, well away from both the top disconnect and the upper electrode. This work involved extensive processing inside a glovebox with <0.5 ppm oxygen. Based on previous work,[45] we expect considerable variation below this down to <0.1 ppm, and it is reasonable to assume that higher QY here correlates with the lowest achievable oxygen level. We note that for one of the high-QY samples (5.5 min annealing time in Figure 4), all the flakes between the electrodes were collected, suggesting that under sufficient oxygen shielding, the working collection length can be much higher than 5 cm. After 2 h, the plasma was turned off, and the reactor was filled with the carrier gas to establish positive pressure. The filter was then isolated from the reactor setup, cleaned, reinstalled, and vacuum-purged for three cycles prior to resuming gas flow. The sample was then annealed in the plasma with the carrier gas flowing, but no precursor, for a predetermined amount of time, after which heat was applied externally with a heat gun to release the flakes from the reactor surface for subsequent transport to the filter. For properly prepared reactors, this last step took less than 5 min, and the precise release time was added to the preplanned annealing time to get the total annealing interval. Upon release, the flakes immediately lighten in color even in the absence of plasma, but liberating the flakes in the presence of plasma was critical to obtaining the optimal spectral shape and QY. A typical 2 h run would yield about 20 mg of raw flakes that could be processed multiple times into passivated suspensions. If flakes from the entire reactor are collected, the mass yield is much higher than this, and we expect mass yield to improve as the level of shielding improves.

The filter apparatus with the collected material was isolated under positive pressure and transferred to a glovebox for further processing. The flakes and 3 mL of mesitylene were charged in a microwave reaction vial and sonicated for 4 h total (60 min intervals with 30 min cooling between them) using a Cole Parmer CPX 130 tip ultrasonicator operating at 130 W (80% power). The mixture was then spun for 10 min at 15,000 rpm in an Eppendorf 5424 desktop centrifuge before extracting a 2 mL supernatant fraction into a clean microwave reaction vial. Following this, 0.4 mL of 1-dodecene was added to the vial, which was subsequently crimp-sealed and heated to 185 °C for 4 h for thermal hydrosilylation. All synthesis and processing steps were performed in oxygen-shielded environments, and all solvents underwent freeze−pump−thaw degassing prior to use.

Photoluminescence Spectroscopy. PL QY was measured with an integrating sphere fiber-coupled through a bifurcated UV/vis and Vis/NIR fiber to Ocean Optics QE65000 and NIRQ512 spectrometers (350−1700 nm available detection), predominantly with 375 nm CW laser excitation at 4.2 mW, but also with 365 nm excitation at 1 mW and a 15 mW 473 nm CW laser operated at low power. The spectral shape was instrument-corrected using the blackbody emission from a tungsten filament as a reference, and the QY was calibrated against multiple standards spanning the visible spectrum. QY was measured at varied SiC NC concentrations with reported values measured in the dilute limit. For PL lifetime, modulated pulsed excitation was delivered with a fiber-coupled pulsed UV laser (Advanced Laser Diode Systems, PiL037, 375 nm, 30 ps pulse width, 140 mW peak power, 1 kHz modulation) fiber-coupled to a photomultiplier tube. A 10× objective was used in EPI illumination. Measurements as a function of NC concentration (Figure 1l) show no statistical change in lifetime until the fully dried state, where the lifetime is slightly (∼30%) larger than that of the colloid. All lifetime measurements were performed on concentrated but not fully dried suspensions, except for the low-QY fractions in Figure 3 (which were fully dried). QYs reported here are those measured concurrently with the lifetime. For example, the 10 min-annealing time sample in Figure 4 initially gave a QY of ∼70%, but despite continuous shielding, this value had relaxed to 60% by the time lifetime was measured. Over the course of nearly a year, the measured value further relaxed to ∼55%. Of note, the high-QY suspensions show an instantaneous drop in QY upon opening the vial in air, which is similar to the behavior reported for Si NCs.[45]

DGU Size Purification. Size purification of the passivated NCs was performed in a Beckman Coulter Optima L-80 XP ultracentrifuge using a five-layer step gradient of 10%, 30%, 50%, 70%, and 90% hexane in toluene by volume. Custom polyvinylidene-fluoride (Kynar) ultracentrifuge tubes were obtained from Seton Scientific. The step gradient was layered using a pipet, with subsequent layers deposited in the order of decreasing density. A 0.3 mL solution of concentrated colloidal SiC NCs (in roughly 1:1 mesitylene:dodecene) was layered on top of the gradient, and the tube was immediately transferred to a SW-41 Ti swinging-bucket rotor and centrifuged for 44 h at 30,000 rpm and 10 °C. After the centrifuge run was complete, fractions were extracted in a nitrogen-filled glovebox using a robotic pump system mounted on a micromanipulator.

For spherical NCs (subscript "s") in a fluid of uniform density, sedimentation velocity maps onto depth in the centrifuge tube (or fraction number f) and scales as R_s^2 where R_s is the NC radius [$v_s = 2\Delta\rho_s GR^2/(9\eta_s)$, with G being the centripetal acceleration, $\Delta\rho$ being the density contrast between the colloid and solvent, and η being the solvent viscosity]. This gives $R \sim f^{1/2}$, whereas experiments in a density gradient[56] give $R \sim f^{1/4}$. For disk-shaped NCs (subscript "d"), sedimentation velocity scales as $R_d\, h$ [$v_d = 3\pi\Delta\rho_d GR_d h/(32\eta_d)$], and for uniform solvent density, we thus expect $Rh \sim f$. In contrast, experiments in a density gradient give $Rh \sim f^{1.45}$ (Figure S4). Qualitatively, we expect a thin disk to have strong viscous effects but weak buoyant effects ($h \to 0$) and thus require a longer spin time. The phenomenological trends support this with $f \sim R_s^4$ and $f \sim (R_d h)^{0.7}$ for spheres and disks, respectively. The sedimentation profile in a density gradient requires numerical solutions of the Lamm equation,[45] but we can rationalize the trends for uniform solvent density. Comparable separation implies $v_d T_d \approx v_s T_s$, where T is the spin time, which gives $T_d \approx (64/27\pi)(\Delta\rho_s/\Delta\rho_d)(\eta_d/\eta_s)(R_s^2/R_d h)T_s$, with the dominant terms being $\Delta\rho_s/\Delta\rho_d$ and $R_s^2/R_d h$. For $R_s \approx R_d \approx 4$ nm and $h \approx 1$ nm, the latter term is on the order of 4, but the former dominates because the effective density of a thin SiC disk is governed by the ligand shell (*i.e.*, $\Delta\rho_d \to 0$).

TEM. Samples were drop-cast on PELCO single-layer graphene lacey carbon 300 mesh copper grids, dried in air for roughly 1 h, and then placed under vacuum at ambient temperature for 24 h. The vacuum oven temperature was then set to 100 °C for 24 h and finally to 200 °C for at least 24 h to remove all the unbound ligand. The drying protocol under heat is what triggers aggregation and self-assembly in sufficiently concentrated suspensions, with more dilute suspensions being used for sizing. HRTEM images were collected with a JEOL JEM2100 LaB6 transmission electron microscope equipped with a Gatan Orius SC1000 CCD camera, and ImageJ was used for sizing.

EDS. Samples were attached to aluminum mounts using double-stick carbon adhesive tabs or tape (Ted Pella, Redding, California) and then coated with a conductive layer of carbon in a high-vacuum evaporative coater (Cressington 208c, Ted Pella). Images were obtained with a JEOL JSM-7600F scanning electron microscope (JEOL). Energy dispersive spectroscopy (EDS) information was acquired using an UltraDry silicon drift X-ray detector and a Pathfinder X-ray Microanalysis System (Thermo Fisher Scientific).

AFM. SiC NC DGU fractions in toluene/hexane straight from the gradient were spin-coated on polished Si wafers for AFM. A fraction was added over a 5 s interval at 300 rpm, and the speed was then ramped to 1000 rpm for 5 s. The wafer was dried under a vacuum at 200 °C for 24 h and imaged with an NT-MDT INTEGRA atomic force microscope. ImageJ was used for the thickness analysis. The ligand contribution to effective NC disk thickness (h_L) is obtained by comparing the XRD thickness for the colloid in Figure 2c (0.83 nm) with the mean AFM thickness from the inset of Figure 2g (1.06 nm), which gives h_L = 0.23 nm (total). For $h \geq 0.5$ nm, thickness h (Figures 3 and 5) can then be approximately converted to the layer number as $n = (h - h_L)/a$, where a = 0.24 nm from Figure 2h. For fraction numbers corresponding to $h \leq 0.5$ nm, the fractions are presumed to contain "monolayers" of varied lateral sizes $2R$, along with small impurities such as unbound ligand.

Nanocrystal Characterization. Raman spectroscopy was performed with a HORIBA Jobin Yvon LabRAM ARAMIS confocal imaging system using 532 nm excitation with 10 and 50× objectives on dried films. A reflecting sample support was used to simultaneously collect both forward and backscattered light, which boosts the signal and accommodates a larger number of Raman selection rules for potentially aligned NCs in the dried films. Diffuse reflectance XRD data were collected from dried samples using a Bruker D8 Discover X-ray diffractometer, with the substrate background measured and removed. FTIR spectra were collected in reflection using a Thermo Scientific Nicolet 8700 instrument with attenuated total reflectance (ATR) capabilities. X-ray photoelectron spectroscopy (XPS) data were collected using a Thermo Scientific K-α XPS system.

ASSOCIATED CONTENT

Supporting Information

The Supporting Information is available free of charge at https://pubs.acs.org/doi/10.1021/acsnano.4c08052.

Additional SEM; TEM; AFM; PL; absorption; Raman; XPS; FTIR; and simulation results (PDF)

AUTHOR INFORMATION

Corresponding Author

Erik K. Hobbie − *Materials & Nanotechnology Program, North Dakota State University, Fargo, North Dakota 58108, United States; Department of Physics and Department of Coatings & Polymeric Materials, North Dakota State University, Fargo, North Dakota 58108, United States;* orcid.org/0000-0001-6158-8977; Email: erik.hobbie@ndsu.edu

Authors

Salim A. Thomas − *Materials & Nanotechnology Program, North Dakota State University, Fargo, North Dakota 58108, United States*

Naif S. Alharthi − *Materials & Nanotechnology Program, North Dakota State University, Fargo, North Dakota 58108, United States*

Reed J. Petersen − *Department of Physics, North Dakota State University, Fargo, North Dakota 58108, United States*

Ahmed Aldrees − *Department of Physics, North Dakota State University, Fargo, North Dakota 58108, United States*

Sakurako Tani − *Department of Physics, North Dakota State University, Fargo, North Dakota 58108, United States*

Kenneth J. Anderson − *Department of Chemistry & Biochemistry, North Dakota State University, Fargo, North Dakota 58108, United States*

Joseph Granlie − *Department of Physics, North Dakota State University, Fargo, North Dakota 58108, United States*

Todd A. Pringle − *Materials & Nanotechnology Program, North Dakota State University, Fargo, North Dakota 58108, United States*

Scott A. Payne − *Materials & Nanotechnology Program, North Dakota State University, Fargo, North Dakota 58108, United States*

Yongki Choi − *Department of Physics, North Dakota State University, Fargo, North Dakota 58108, United States;* orcid.org/0000-0001-8890-8344

Dmitri S. Kilin − *Department of Chemistry & Biochemistry, North Dakota State University, Fargo, North Dakota 58108, United States;* orcid.org/0000-0001-7847-5549

Complete contact information is available at: https://pubs.acs.org/10.1021/acsnano.4c08052

Notes

The authors declare no competing financial interest.

REFERENCES

(1) Gutiérrez, H. R. Two-Dimensional Layered Materials Offering Expanded Applications in Flatland. *ACS Appl. Nano Mater.* **2020**, *3*, 6134−6139.

(2) Zhao, X.; Song, P.; Wang, C.; Riis-Jensen, A. C.; Fu, W.; Deng, Y.; Wan, D.; Kang, L.; Ning, S.; Dan, J.; Venkatesan, T.; Liu, Z.; Zhou, W.; Thygesen, K. S.; Luo, X.; Pennycook, S. J.; Loh, K. P. Engineering Covalently Bonded 2D Layered Materials by Self-Intercalation. *Nature* **2020**, *581*, 171−177.

(3) Yao, J.; Yang, G. 2D Layered Material Alloys: Synthesis and Application in Electronic and Optoelectronic Devices. *Adv. Sci.* **2022**, *9*, No. 2103036.

(4) Ryan, B. J.; Roling, L. T.; Panthani, M. G. Anisotropic Disorder and Thermal Stability of Silicane. *ACS Nano* **2021**, *15*, 14557−14569.

(5) Shi, Z.; Zhang, Z.; Kutana, A.; Yakobson, B. I. Predicting Two-Dimensional Silicon Carbide Monolayers. *ACS Nano* **2015**, *9*, 9802−9808.

(6) Polley, C. M.; Fedderwitz, H.; Balasubramanian, T.; Zakharov, A. A.; Yakimova, R.; Bäcke, O.; Ekman, J.; Dash, S. P.; Kubatkin, S.; Lara-Avila, S. Bottom-Up Growth of Monolayer Honeycomb SiC. *Phys. Rev. Lett.* **2023**, *130*, No. 076203.

(7) Lin, S. S. Light-Emitting Two-Dimensional Ultrathin Silicon Carbide. *J. Phys. Chem. C* **2012**, *116*, 3951−3954.

(8) Susi, T.; Skákalová, V.; Mittelberger, A.; Kotrusz, P.; Hulman, M.; Pennycook, T. J.; Mangler, C.; Kotakoski, J.; Meyer, J. C. Computational Insights and the Observation of SiC Nanograin Assembly: Towards 2D Silicon Carbide. *Sci. Rep.* **2017**, *7*, No. 4399.

(9) Chabi, S.; Guler, Z.; Brearley, A. J.; Benavidez, A. D.; Luk, T. S. The Creation of True Two-Dimensional Silicon Carbide. *Nanomaterials* **2021**, *11*, 1799−1884.

(10) Castelletto, S.; Peruzzo, A.; Bonato, C.; Johnson, B. C.; Radulaski, M.; Ou, H.; Kaiser, F.; Wrachtrup, J. Silicon Carbide Photonics Bridging Quantum Technology. *ACS Photonics* **2022**, *9*, 1434−1457.

(11) Henderson, E. J.; Veinot, J. G. C. From Phenylsiloxane Polymer Composition to Size-Controlled Silicon Carbide Nanocrystals. *J. Am. Chem. Soc.* **2009**, *131*, 809−815.

(12) Askari, S.; Ul Haq, A.; Macias-Montero, M.; Levchenko, I.; Yu, F.; Zhou, W.; Ostrikov, K.; Maguire, P.; Svrcek, V.; Mariotti, D. Ultra-Small Photoluminescent Silicon-Carbide Nanocrystals by Atmospheric-Pressure Plasmas. *Nanoscale* **2016**, *8*, 17141−17149.

(13) Haq, A. U.; Buerkle, M.; Askari, S.; Rocks, C.; Ni, C.; Švrček, V.; Maguire, P.; Irvine, J. T. S.; Mariotti, D. Controlling the Energy-Level Alignment of Silicon Carbide Nanocrystals by Combining Surface Chemistry with Quantum Confinement. *J. Phys. Chem. Lett.* **2020**, *11* (5), 1721−1728.

(14) Wang, C.; Zhou, J.; Song, M.; Lu, Z.; Chen, X.; Zheng, Y.; Xia, W. Synthesis of Ultrafine Silicon Carbide Nanoparticles using Nonthermal Arc Plasma at Atmospheric Pressure. *J. Am. Ceram. Soc.* **2021**, *104*, 3883−3894.

(15) Galář, P.; Stuchlík, J.; Müller, M.; Kočka, J.; Kůsová, K. Highly Spherical SiC Nanoparticles Grown in Nonthermal Plasma. *Plasma Processes Polym.* **2022**, *19*, No. 2100127.

(16) Petersen, R. J.; Thomas, S. A.; Anderson, K. J.; Pringle, T. A.; May, S.; Hobbie, E. K. Nonthermal Plasma Synthesis of Colloidal Silicon-Carbide Nanocrystals: Surface Chemistry and Quantum Confinement. *J. Phys. Chem. C* **2022**, *126*, 12935−12943.

(17) Huang, J.-J.; Militzer, C.; Wijayawardhana, C.; Forsberg, U.; Ojamäe, L.; Pedersen, H. Controlled CVD Growth of Highly ⟨111⟩-Oriented 3C-SiC. *J. Phys. Chem. C* **2022**, *126*, 9918−9925.

(18) Beke, D.; Janosi, T. Z.; Somogyi, B.; Major, D. A.; Szekrenyes, Z.; Erostyak, J.; Kamaras, K.; Gali, A. Identification of Luminescence Centers in Molecular-Sized Silicon Carbide Nanocrystals. *J. Phys. Chem. C* **2016**, *120* (1), 685−691.

(19) Beke, D.; Fucikova, A.; Janosi, T. Z.; Karolyhazy, G.; Somogyi, B.; Lenk, S.; Krafcsik, O.; Czigany, Z.; Erostyak, J.; Kamaras, K.; Valenta, J.; Gali, A. Direct Observation of Transition from Solid-State to Molecular-Like Optical Properties in Ultrasmall Silicon Carbide Nanoparticles. *J. Phys. Chem. C* **2018**, *122* (46), 26713−26721.

(20) Guo, X. X.; Zhang, Y. M.; Fan, B. L.; Fan, J. Y. Quantum Confinement Effect in 6H-SiC Quantum Dots Observed via Plasmon-Exciton Coupling-Induced Defect-Luminescence Quenching. *Appl. Phys. Lett.* **2017**, *110* (12), No. 123104.

(21) Guo, X. X.; Chen, X. F.; Fan, B. L.; Zhang, Y. M.; Fan, J. Y. Photon Absorption and Emission Properties of 7 Angstrom SiC Nanoclusters: Electronic Gap, Surface State, and Quantum Size Effect. *Appl. Phys. Lett.* **2016**, *109* (1), No. 013104.

(22) Beke, D.; Szekrenyes, Z.; Czigany, Z.; Kamaras, K.; Gali, A. Dominant Luminescence is not due to Quantum Confinement in Molecular-Sized Silicon Carbide Nanocrystals. *Nanoscale* **2015**, *7*, 10982−10988.

(23) Guo, X.; Dai, D.; Fan, B.; Fan, J. Experimental Evidence of $\alpha \rightarrow \beta$ Phase Transformation in SiC Quantum Dots and their Size-Dependent Luminescence. *Appl. Phys. Lett.* **2014**, *105*, No. 193110.

(24) Fan, J.; Li, H.; Wang, J.; Xiao, M. Fabrication and Photoluminescence of SiC Quantum Dots Stemming from 3C, 6H, and 4H Polytypes of Bulk SiC. *Appl. Phys. Lett.* **2012**, *101*, No. 131906.

(25) Fan, J. Y.; Li, H. X.; Wang, Q. J.; Dai, D. J.; Chu, P. K. UV-Blue Photoluminescence from Close-Packed SiC Nanocrystal Film. *Appl. Phys. Lett.* **2011**, *98*, No. 081913.

(26) Fan, J.; Li, H.; Jiang, J.; So, L. K. Y.; Lam, Y. W.; Chu, P. K. 3C−SiC Nanocrystals as Fluorescent Biological Labels. *Small* **2008**, *4*, 1058−1062.

(27) Dai, D. J.; Zhang, C. Y.; Wang, L.; Wang, Y.; Zhang, B. H.; Deng, K. M.; Lu, W.; Fan, J. Y. Reversible/Irreversible Photobleaching of Fluorescent Surface Defects of SiC Quantum Dots: Mechanism and Sensing of Solar UV Irradiation. *Adv. Mater. Interfaces* **2019**, *6* (11), No. 1900272.

(28) Castelletto, S.; Barbiero, M.; Charnley, M.; Boretti, A.; Gu, M. Imaging with Nanometer Resolution Using Optically Active Defects in Silicon Carbide. *Phys. Rev. Appl.* **2020**, *14* (3), No. 034021.

(29) Castelletto, S.; Johnson, B. C.; Zachreson, C.; Beke, D.; Balogh, I.; Ohshima, T.; Aharonovich, I.; Gali, A. Room Temperature Quantum Emission from Cubic Silicon Carbide Nanoparticles. *ACS Nano* **2014**, *8*, 7938−7947.

(30) Castelletto, S.; Almutairi, A. F. M.; Thalassinos, G.; Lohrmann, A.; Buividas, R.; Lau, D. W. M.; Reineck, P.; Juodkazis, S.; Ohshima, T.; Gibson, B. C.; Johnson, B. C. Fluorescent Color Centers in Laser Ablated 4H-SiC Nanoparticles. *Opt. Lett.* **2017**, *42* (7), 1297−1300.

(31) Lu, W.; Ou, Y.; Fiordaliso, E. M.; Iwasa, Y.; Jokubavicius, V.; Syväjärvi, M.; Kamiyama, S.; Petersen, P. M.; Ou, H. White light emission from fluorescent SiC with porous surface. *Sci. Rep.* **2017**, *7*, No. 9798.

(32) Wei, Y.; Ou, H. Photoluminescence Quantum Yield of Fluorescent Silicon Carbide Determined by an Integrating Sphere Setup. *ACS Omega* **2019**, *4*, 15488−15495.

(33) Rosso, M.; Arafat, A.; Schroen, K.; Giesbers, M.; Roper, C. S.; Maboudian, R.; Zuilhof, H. Covalent Attachment of Organic Monolayers to Silicon Carbide Surfaces. *Langmuir* **2008**, *24*, 4007−4012.

(34) Alekseev, S.; Shamatulskaya, E.; Volvach, M.; Gryn, S.; Korytko, D.; Bezverkhyy, I.; Iablokov, V.; Lysenko, V. Size and Surface Chemistry Tuning of Silicon Carbide Nanoparticles. *Langmuir* **2017**, *33*, 13561−13571.

(35) Dhar, S.; Seitz, O.; Halls, M. D.; Choi, S.; Chabal, Y. J.; Feldman, L. C. Chemical Properties of Oxidized Silicon Carbide Surfaces upon Etching in Hydrofluoric Acid. *J. Am. Chem. Soc.* **2009**, *131*, 16808−16813.

(36) Rashid, M.; Tiwari, A. K.; Goss, J. P.; Rayson, M. J.; Briddon, P. R.; Horsfall, A. B. Surface-State Dependent Optical Properties of OH-, F-, and H-Terminated 4H-SiC Quantum Dots. *Phys. Chem. Chem. Phys.* **2016**, *18* (31), 21676−21685.

(37) Ding, H.; Li, X.-H.; Chen, X.-B.; Wei, J.-S.; Li, X.-B.; Xiong, H.-M. Surface States of Carbon Dots and their Influences on Luminescence. *J. Appl. Phys.* **2020**, *127*, No. 231101.

(38) Liu, M. L.; Chen, B. B.; Li, C. M.; Huang, C. Z. Carbon Dots: Synthesis, Formation Mechanism, Fluorescence Origin and Sensing Applications. *Green. Chem.* **2019**, *21*, 449−471.

(39) Lim, S. Y.; Shen, W.; Gao, Z. Carbon Quantum Dots and their Applications. *Chem. Soc. Rev.* **2015**, *44*, 362−381.

(40) Du, J.; Xu, N.; Fan, J.; Sun, W.; Peng, X. Carbon Dots for In Vivo Bioimaging and Theranostics. *Small* **2019**, *15*, No. 1805087.

(41) Yuan, F.; Wang, Z.; Li, X.; Li, Y.; Tan, Z. A.; Fan, L.; Yang, S. Bright Multicolor Bandgap Fluorescent Carbon Quantum Dots for Electroluminescent Light-Emitting Diodes. *Adv. Mater.* **2017**, *29*, No. 1604436.

(42) Sciortino, A.; Cannizzo, A.; Messina, F. Carbon Nanodots: A Review—From the Current Understanding of the Fundamental Photophysics to the Full Control of the Optical Response. *J. Carbon Res.* **2018**, *4*, No. 67.

(43) Sekiya, R.; Uemura, Y.; Murakami, H.; Haino, T. White-Light-Emitting Edge-Functionalized Graphene Quantum Dots. *Angew. Chem., Int. Ed.* **2014**, *53*, 5619−5623.

(44) Ding, H.; Yu, S.-B.; Wei, J.-S.; Xiong, H.-M. Full-Color Light-Emitting Carbon Dots with a Surface-State-Controlled Luminescence Mechanism. *ACS Nano* **2016**, *10*, 484−491.

(45) Pringle, T. A.; Hunter, K. I.; Brumberg, A.; Anderson, K.; Fagan, J. A.; Thomas, S. A.; Petersen, R. J.; Sefannaser, M.; Han, Y.; Brown, S. L.; Kilin, D. S.; Schaller, R. D.; Kortshagen, U.; Boudjouk, P.; Hobbie, E. K. Bright Silicon Nanocrystals from a Liquid Precursor: Quasi-Direct Recombination with High Quantum Yield. *ACS Nano* **2020**, *14*, 3858−3867.

(46) Sefannaser, M.; Thomas, S. A.; Anderson, K. J.; Petersen, R. J.; Brown, S. L.; Boudjouk, P. R.; Pringle, T. A.; Hobbie, Erik K. Radiative Relaxation in Luminescent Silicon Nanocrystal Thiol-Ene Composites. *J. Phys. Chem. C* **2021**, *125*, 5824−5831.

(47) Brown, S. L.; Miller, J. B.; Anthony, R. J.; Kortshagen, U. R.; Kryjevski, A.; Hobbie, E. K. Abrupt Size Partitioning of Multimodal Photoluminescence Relaxation in Monodisperse Silicon Nanocrystals. *ACS Nano* **2017**, *11*, 1597−1603.

(48) Miller, J. B.; Harris, J. M.; Hobbie, E. K. Purifying Colloidal Nanoparticles through Ultracentrifugation with Implications for Interfaces and Materials. *Langmuir* **2014**, *30*, 7936−7946.

(49) Miller, J. B.; Hobbie, E. K. Nanoparticles as Macromolecules. *J. Polym. Sci., Part B: Polym. Phys.* **2013**, *51*, 1195−1208.

(50) Sohier, T.; Gibertini, M.; Calandra, M.; Mauri, F.; Marzari, N. Breakdown of Optical Phonons' Splitting in Two-Dimensional Materials. *Nano Lett.* **2017**, *17*, 3758−3763.

(51) De Luca, M.; Cartoixà, X.; Indolese, D. I.; Martín-Sánchez, J.; Watanabe, K.; Taniguchi, T.; Schönenberger, C.; Trotta, R.; Rurali, R.; Zardo, I. Experimental Demonstration of the Suppression of Optical Phonon Splitting in 2D Materials by Raman Spectroscopy. *2D Mater.* **2020**, *7*, No. 035017.

(52) Granlie, J. D.; Hobbie, E. K.; Kilin, D. S. Formation and Luminescence of Single Oxygen Impurities on the Surface of SiC Nanocrystals. *J. Phys. Chem. Lett.* **2023**, *14*, 6202−6208.

(53) Chen, I. Y.; da Silva, J. C.; Balazs, D. M.; Smeaton, M. A.; Kourkoutis, L. F.; Hanrath, T.; Clancy, P. The Role of Dimer Formation in the Nucleation of Superlattice Transformations and its Impact on Disorder. *ACS Nano* **2020**, *14*, 11431−11441.

(54) Batista, C. A. S.; Larson, R. G.; Kotov, N. A. Non-additivity of Nanoparticle Interactions. *Science* **2015**, *350*, No. 1242477.

(55) See, for example, Jingu, N.; Sumida, K.; Hayakawa, T.; Ono, T.; Saitow, K. Ligand Stabilities and Reactivities of Green Photoluminescent Silicon Quantum Dots: Positive Aging in Solution. *Chem. Mater.* **2024**, *36*, 5077−5091.

(56) Forde, A. A.; Thomas, S. A.; Petersen, R. J.; Kilin, D. S.; Hobbie, E. K. Impurity Induced Confinement Effects in Size-Separated Mn-Doped $CsPbCl_3$ Nanocrystals. *Phys. Rev. Mater.* **2024**, *8*, No. 066001.